Proceedings of the 11th ICPMG 2026
11th International Conference on Physical Modelling in Geotechnics
8-12 June 2026, Zurich, Switzerland

Physical modelling of a novel groutless rock anchoring system for floating offshore renewable applications

W. Wang
University of Dundee, Dundee, UK, wwang005@dundee.ac.uk

M. O. Ciantia
University of Dundee, Dundee, UK, m.o.ciantia@dundee.ac.uk
University Milano Bicocca, Milan, Italy, matteo.ciantia@unimib.it

A. Genco
Norwegian Geotechnical Institute, Oslo, Norway, alessio.genco@ngi.no
Formerly University of Dundee, Dundee, UK

P. P. He, C. Davidson
University of Dundee, Dundee, UK, PHe001@dundee.ac.uk, c.s.davidson@dundee.ac.uk

ABSTRACT: This paper presents small-scale physical modelling of a novel groutless rock anchor system for offshore renewable energy applications installed in soft calcarenite rock and, subject to cyclic loading. The rock anchor is characterised by a self-drilling installation process and the mobilisation of resistance through mechanical interlocking with the surrounding rock via an expandable bottom finger. This mechanical interlock is activated by the application of pretension, which is induced by applying torque at the top end of the anchor. In the present physical modelling regime, the anchor was modelled by a combination of a Hilti HDA-P M10 and a bespoke top taper designed to include a pad eye and to accommodate an axial load cell to measure the pretension. At lower cyclic loading amplitudes, pretension loss was limited, loading stiffness remained stable, and displacement accumulation was minimal and stabilised with cycle number. In contrast, higher cyclic loading amplitudes resulted in substantial pretension loss, progressive stiffness degradation, and significant displacement accumulation.

1 INTRODUCTION

Offshore renewable energy (ORE) applications are going to be deployed in both soily and rocky seabed locations. While gravity-based anchors are a solution for rocks, it is less cost-effective with higher loading when compared to embedded anchors. To sustain tensile loads, conventional embedded anchor solutions in rocks require the use of cement-based grouts (Brown 2015; Finnie et al. 2019; Grindheim et al. 2023; Sandrini et al. 2022). Their use in deeper waters is therefore problematic as installation and decommissioning become extremely difficult and costly. Alternatively, groutless rock anchoring solutions are becoming more attractive for floating ORE applications (ORE Catapult and ARUP 2024).

The rock anchor technology, "Swift Anchor" (SA), investigated in this paper was recently designed by SCHOTTEL Marine Technologies (SMT) (https://schottel-mt.com/) aiming to reduce operation costs and environmental footprint by means of a groutless, and self-drilling solution (Genco 2025). This technology relies on the mechanical interlock between rock and anchor to provide stability in weak and hard rocks (Kaufmann et al 2025). The mechanical interlock is similar to that of undercut anchors, which are typically used in steel-concrete connections (Cook et al. 1989) and can be also used in rocks (Jonak et al. 2021).

The main components of the SA include an outer casing with expandable fingers at the base, an upper taper, an anchor nut, and an inner stem fitted with a sacrificial drill bit (Figure 1). The top taper has a pad eye which allows the connection between anchor and floating platforms generally through mooring lines. The installation of the anchors is as follows: i) The drill bit, fixed to the base of the anchor, cores into the rocky seabed, forming the required cavity that allows the entire anchor to advance simultaneously. At the drilling stage the inner stem and outer casing are coupled together acting as a single element (Figure 1b). ii) Once reaching the design depth, the inner and outer casing are decoupled. The inner stem is retracted expanding the fingers, undercutting the surrounding rock (Figure 1c). This enables full contact between rock and fingers and create a bottom taper. Whereas a gap between shaft and rock remains, allowing cuttings to be flushed to the surface. iii) Pre-tensioning is then applied by tightening the anchor nut on top, and therefore the top taper and the bottom taper compress the rock between them ensuring the anchor stability (Figure 1c). This anchoring system also has a potential for relatively easy reuse by releasing the pre-tension followed by lowering the inner stem and retrieving. In contrast, conventional grouted rock anchors are typically destructively decommissioned by cutting the anchor below the rock surface and leaving it in place.

Recent full-scale field tests have confirmed the reliable deployability of the system and verified that its in-service static holding capacity satisfies the intended design criteria (Kaufmann et al. 2025). In order to optimise the SA design, several laboratory experiments and numerical simulations have been conducted; however, the influences of top taper and pretension have typically been neglected, with most studies focusing predominantly on pure axial loading conditions (Cerfontaine et al. 2021; Genco et al. 2024a; Genco et al. 2024b). More recently, numerical and experimental investigations have incorporated pretension effects and examined the multidirectional performance of SAs (Ciantia et al. 2026; Genco 2025).

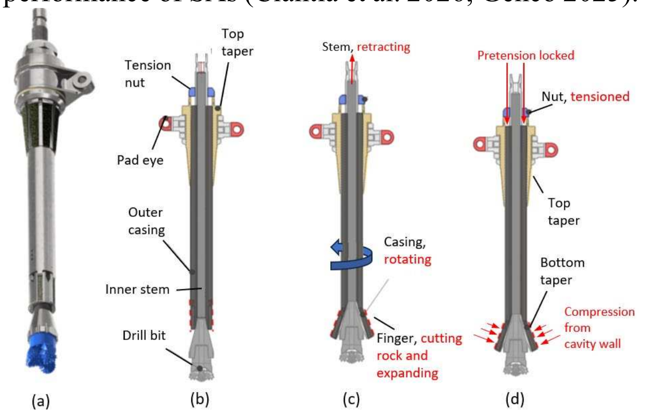

Figure 1 (a) 3D visualisation of the Swift Anchor, and schematic illustration of the installation process: (b) before inner stem retraction and (c) after inner stem retraction (after Genco 2025)

One of the key considerations for offshore anchor design, in both rocks and soils, is to assess the cyclic loading performance. For conventional pile anchors in soft rocks, cyclic loading has been shown to lead to permanent displacement accumulation and variation of anchor system capacity and stiffness (Buckley et al. 2024; Riccio 2025). Preliminary experimental investigation of SAs in concrete by Genco (2025) showed that loading-unloading cycles may result in a reduction in the pretension, raising an extra consideration for SA design regarding cyclic loading.

This study adopts the experimental set-up for SAs in concrete (Genco 2025) and further extends it to investigate SA behaviour in soft rock. Pure axial loading is first considered to isolate and quantify the effects of pretension on the rock mass. The performance of SAs under cyclic loading is then examined for a loading direction inclined at 30° to the ground surface. The cyclic evolution of permanent displacement, pretension force, and loading stiffness is analysed and discussed. This research forms part of an ongoing experimental programme, within which the influences of loading direction and initial pretension magnitude will be systematically investigated.

2 PHYSICAL MODELLING

2.1 Calcarenite rock

The anchors were installed in calcarenite blocks from a quarry in Melpignano (LE), Italy. The rock blocks are in cuboidal and 36 × 36 × 20 cm in dimension. Laboratory element tests were conducted on samples made from the blocks, and the key rock properties are shown in Table 1.

Table 1. Properties of calcarenite tested

Property	Value
Dry unit weight, γ	16.0 kN/m^3
Unconfined Compressive Strength, σ_{UCS}	17.0 MPa
Young's modulus, E	0.87 MPa
Brazilian Tensile Strength, σ_t	2.1 MPa

2.2 Anchor model

The Swift Anchor was physically modelled using an undercut anchor combined with a top taper and a pad-eye, as shown in Figure 2. It should be noted that present study did not aim to reproduce the full-scale prototype geometrically, but rather to capture and investigate the pretension mechanisms. While certain geometric features are comparable to the full-scale anchor, strict proportional similarity was not imposed. The model should therefore be regarded as a mechanism-representative configuration rather than a geometrically scaled replica.

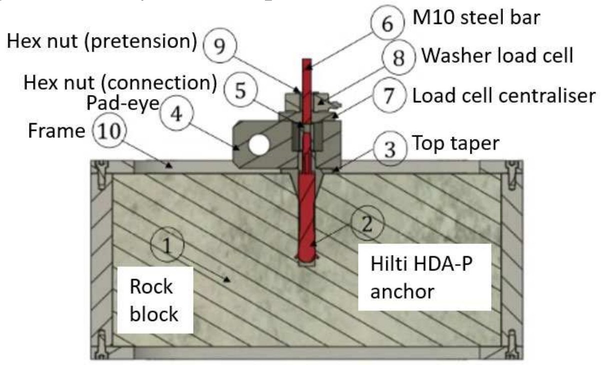

Figure 2 Cross section of the physical modelling set-up for a Swift anchor (after Genco 2025)

The undercut anchors adopted in this study were Hilti HDA-P M10 (https://www.hilti.co.uk/) (Part 2, Figure 2, and Figure 3). Each of the Hilit anchor had an inner stem, with an expandable undercutting mechanism at the base, and an M10 threaded section at the top. To install the anchor, a hammer drill is applied on the top of the outer casing and consequently the casing bottom is progressively open and cuts and finally interlocks with surrounding rock. Details of the installation procedure are provided later in this section. The anchor finger embedment depth, H = 100 mm and the finger diameter D = 25 mm when fully opened, resulting in an embedment depth ratio H/D = 4. Whilst the full-scale SA has a larger H/D = 5.6 (H = 1.8 m and D = 0.32 mm).

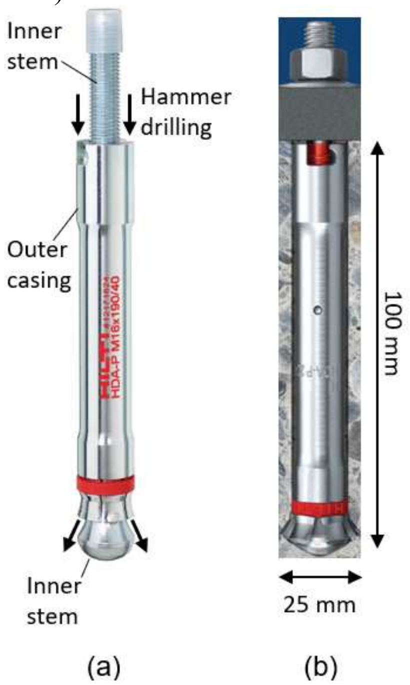

Figure 3 A Hilti HDA-P M10 anchor (a) before installation (b) after installation

The top taper (Part 3, Figure 2) had an inclination angle of 14° and a height of 20 mm (full-scale SA dimensions are 14° and 4 mm, respectively). The inner hole of the taper was designed to encase the Hilti anchor.

To accommodate the Hilti anchor and the top taper in the rock, the installation procedure is as follows: (i) A vertical hole was drilled at the centre of each rock block using a hand-held drill fitted with the standard drill bit specified for the Hilti HDA-P M10 anchor. A drill guide was employed to ensure verticality. Both the drill bit and the resulting hole had a diameter of 10 mm, which is 1.5 mm greater than the outer casing diameter of the anchor (0.25 m hole diameter and 0.22 m casing diameter for a full-scale SA). (ii) Drilling a conical opening at the top of the hole, using a bespoke conical drill bit. The drill bit had an inclination angle of 29°, consistent with the top taper geometry. It comprised a three-quarter conical body fabricated by 3D printing and steel cutting elements accommodated within the remaining open quarter. (iii) The hole was cleaned using compressed air, after which the anchor was inserted. (iv) Applying HILTI TE 30 AVR rotary hammer drill on the outer casing through a Hilti standard setting tool, to drive the casing downwards and to open the finger. (v) Finally, placing the top taper and pad-eye as well as any other parts as shown in Figure 2.

The pad-eye (Part 4) is geometrically scaled down from the full-scale counterpart. The hole within the pad-eye was for the insertion of the top taper. The pad-eye leads to a load application point located at 55 mm lateral eccentricity and 32.5 mm as axial eccentricity.

To apply a pretension force, the threaded head of the HILTI anchor was connected to an extension threaded bar (Part 6) by a hexagon nut (Part 5). The extension bar was through the central holes of a load cell centraliser and a PCM C-FW-M14 Compressive Force Washer load cell (Part8), which was positioned above the pad-eye. A second hexagonal nut (Part 5) was installed above the load cell, and torque was applied to this nut to induce tension in the anchor–extension bar assembly, thereby simulating the pretension in the SA. The magnitude of the applied pretension was taken as the force measured by the washer load cell.

2.3 Pretension

As illustrated in Section 2.1, pretension was applied to the anchor by manually applying torque to the hexagonal nut located above the washer-type compressive load cell (Figure 2, Part 9). A calibrated torque wrench with a maximum capacity of 112 Nm was used. The washer load cell reading, taken as the applied pretension force, was recorded continuously throughout the procedure. Torque was applied incrementally in steps of 5 Nm. At each increment, once the target torque was reached and the torque wrench engaged (audible click), the corresponding pretension force was recorded. This procedure enabled the establishment of a torque–pretension relationship for the anchor system.

2.4 Test loading system

The loading system is shown in Figure 4. An Instron 4204® Universal Testing Machine (UTM) was used to apply vertical tensile loading on the pad-eye. The load was transmitted through a chain assembly comprising shackles connecting the loading head of the Instron to the upper end of the chain and additional shackles connecting the lower end of the chain to the pad-eye.

The Instron is equipped with a static load cell with a maximum capacity of ±250 kN, where the 10 mm off-centre loading error was ±0.03%.

Rock blocks, where the anchors were installed in, were accommodated by a customised tilting steel frame, which was originally designed by Schottel Marine Technologies. The frame incorporated a tilting steel box that allowed the inclination of the loading direction relative to the rock surface, enabling the application of inclined loading using the vertically acting Instron machine. The box was attached to the side supports by pins inserted into designated holes, enabling inclinations from 0° to 90° in 15° increments. More details of this frame can be found in Genco (2025).

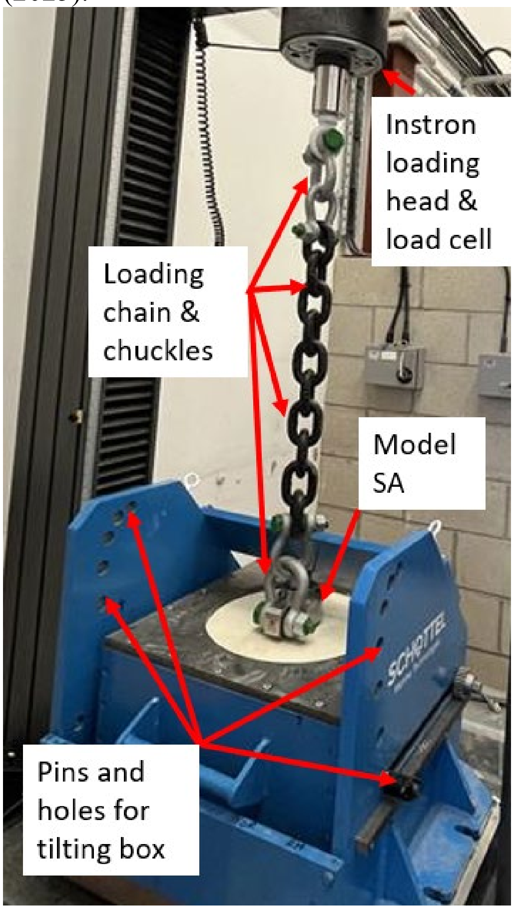

Figure 4 A photograph the bespoke frame, test setup and loading system

3 RESULTS AND DISCUSSION

3.1 Axial loading of a Hilti anchor

Before testing the full model SA, the axial monotonic loading response of a single Hilti anchor without the top tapper neither the pad-eye was assessed. In another words, only Part 1, 2 and 10 shown in Figure 2 were involved, and the Hilti anchor was directly connected to the Instron loading head. Therefore, pretension was not applied. This is in order to establish an appropriate pretension magnitude for subsequent SA tests and to facilitate the interpretation pf the pretension effects. Monotonic loading was applied under displacement control, with the Instron loading head displaced upward at a constant rate of 2 mm/min.

Figure 5 shows the sectioned rock block after tests. Because the rock is soft, the finger only scraped the rock surface locally, without causing any crack initiation or propagation in the surrounding rock mass during axial loading. The axial loading – displacement measured at the Instron loading head is shown in Figure 6. Two tests were conducted and show good consistency. Both tests show that the response becomes relatively non-linear at a loading approximately = 8 kN, which potentially indicates the instigation of local rock damage (i.e. the finger starts to scrape the rock).

Although the tilting steel frame had a rated capacity of 250 kN, the allowable working load of the lifting eye and the Instron adaptor was limited to 25 kN. Consequently, loading was terminated at 25 kN, and the ultimate axial capacity of the Hilti anchor in the calcarenite was not reached in the present tests. Alternatively, an empirical – analytical model (Kim and Cho, 2012) can be used to estimate the ultimate axial capacity F_{ult} (Eq.1):

$$F_{ult} = f_r + W_c \tag{1}$$

This model assumes a cone-shape failure originated from the bottom end of the anchor (the bottom finger in this case) and F_{ult} is a sum of tensile force on the failure surface (f_r) and the weight of the failure cone (W_c), as illustrated in Figure 7. The values of f_r and W_c are calculated from:

$$f_r = \sigma_t \pi H^2 tan\,(\theta/2)/cos\,(\theta/2) \tag{2}$$

$$W_c = \frac{\pi}{3}\gamma H^3 tan^2(\theta/2) \tag{3}$$

where H = embedment depth of the anchor, σ_t = rock tensile strength, γ = rock unit weight, and θ = inclination angle of the failure cone, which can be empirically estimated as 60° for soft rock, as adopted in Figure 5 in this study, and 90° for hard rock.

As shown in Figure 5, is substantially lower than that predicted by the model of Kim and Cho (2012) the working load limitation of the loading system. With further loading, the anchor finger may continuously scrape the rock resulting in a reduction of the anchor embedment depth and consequently the ultimate capacity. Once the capacity is decreased to the current uplift loading, a cone failure is expected to happen. To load the Hilti anchor to an ultimate state would require either an upgraded loading system capable of applying higher forces or testing in a weaker rock material.

However, the primary objective of the axial loading tests was not to reach ultimate failure, but rather to inform the pretension effects. In practice, the applied pretension is not intended to approach the ultimate anchor capacity.

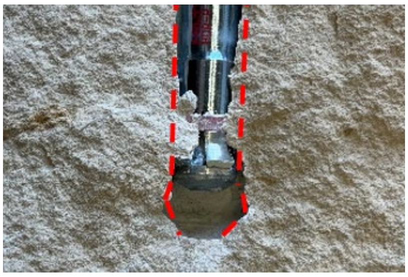

Figure 5 A photograph of the opened rock block around the anchor finger anchor after the axial loading test (the red dashed line indicates the initial anchor position prior to loading)

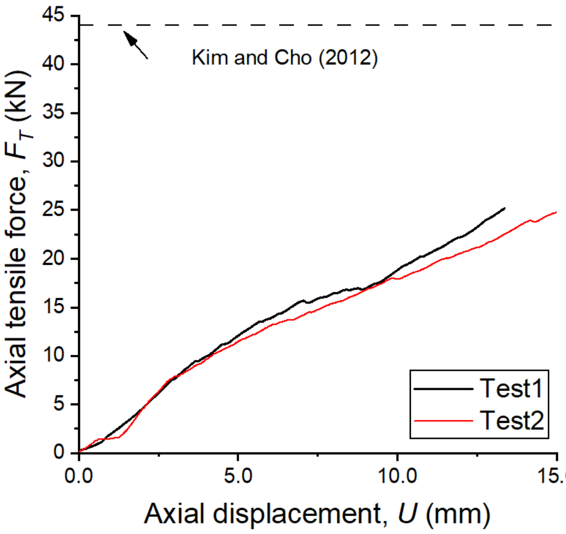

Figure 6 Axial loading – displacement response of a Hilti anchor in the calcarenite

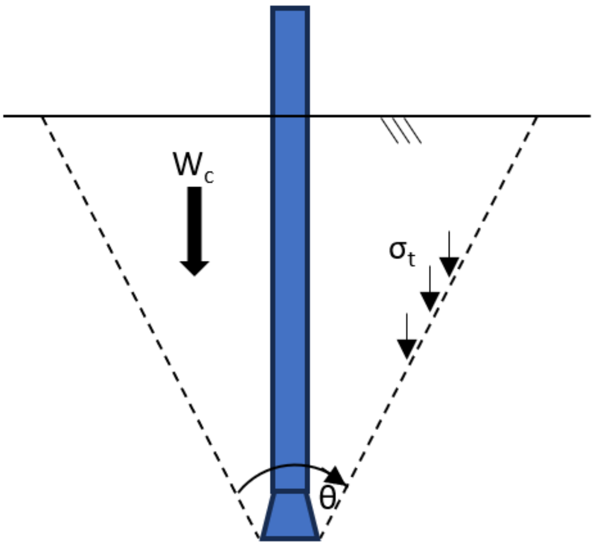

Figure 7 Idealisation of the rock cone failure for an undercut anchor subject to axial tensile loading

3.2 Pretension

To investigate cyclic performance of the SA, another test was conducted on a model using the full experimental setup as shown in Figure 2. Part 2 (the Hilti anchor) and Part 1 (the rock block) consisted of the fresh SA model had not been previously loaded and were therefore not identical to those used in Section 3.1.

The model SA was installed following the whole procedure illustrated in Section 2.2 where pretension was applied. Figure 8 presents the evolution of pretension magnitude with time. The dotted lines and boxed annotations indicate the points at which successive torque levels were reached. Each abrupt increase in pretension corresponds to the application of torque to the hexagonal nut above the compressive load cell using the manual torque wrench (Section 2.3). Upon cessation of nut rotation, a reduction in pretension is observed, potentially indicating relaxation of the nut-thread interaction. After the final torque level of 50 Nm was applied, the system was left under sustained conditions to examine whether a stable pretension level could be achieved. However, even after approximately 40 minutes, the pretension continued to decrease, at a reduced and steady rate (in an order of 10^{-4} kN/s). This relatively long-term relaxation is likely related to creep of the rock or rock-anchor interface, due to the compression of this type of soft rock between tapers. This relaxion may be offset by re-application of pre-tension if required, enabling adjustment and maintenance of stability. This operational flexibility represents an advantage compared to conventional grouted systems, where post-installation adjustment is typically not feasible.

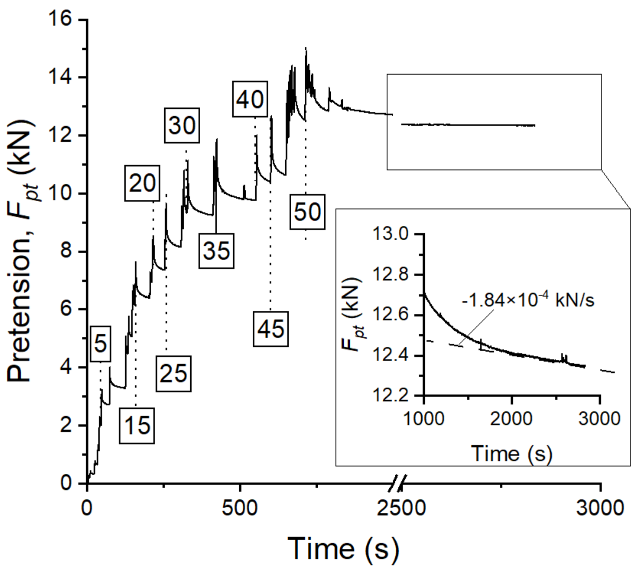

Figure 8 Pretention force varying with time. Numbers in boxes are applied torque in Nm at time (zoomed in shown from time = 1000s to 3000s)

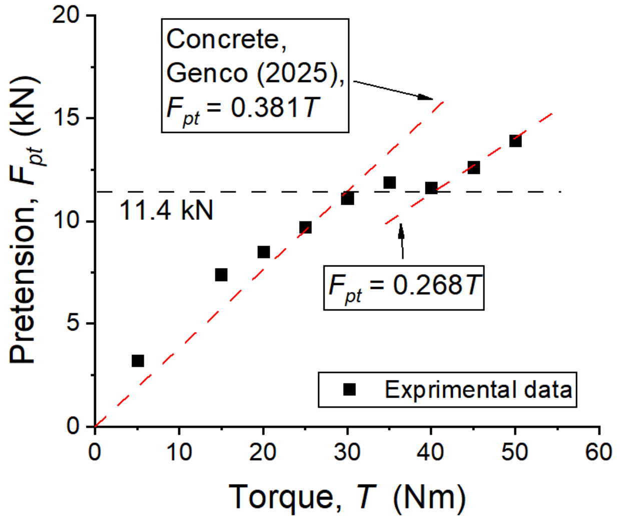

Figure 9 Pretention force – torque response of the model SA: comparison between concrete and the calcarenite

Figure 9 shows force – torque response during applying pretension, with a comparison to previous tests conducted in concrete. Up to a torque of approximately 30 Nm. The initial slope of the pretension–torque relationship is comparable to that reported for concrete (Genco 2025). Between torque levels of 30 Nm and 40 Nm, the pretension force remains approximately constant at around 12.3 kN. Beyond this range, the pretension force increases again with increasing torque, although with a reduced slope compared to the initial linear regime. This observation is consistent with the instigation of non-linear force – displacement response in the Hilti anchor axial loading test (Figure 6), and similarly indicates the onset of localised damage or failure in the surrounding rock.

3.3 Cyclic loading tests

Following the pretension procedure, cyclic loading was conducted in a force-controlled mode, at a constant rate of 5 kN/min. The initial pretension magnitude was 12.3 kN as mentioned in the last section. The pad-eye was loaded at an inclination angle = 30° from the rock block surface, consistent with typical working directions associated with catenary and semi-taut mooring systems. Prior to cyclic loading, a sustained loading of 2.5 kN was first applied on the pad-eye. To maximise the amount of data obtained from a single anchor, cyclic loading was conducted in discrete loading packets. The loading programme is shown in Table 2.

Figure 10 shows the force – displacement during cyclic loading, as well as the evolution of the pretension force. Permanent displacement is accumulated and pretension is reduced with cyclic loading.

Table 2. Cyclic loading programme

Packet No.	Minimum force (kN)	Maximum force (kN)	Number of cycles
I	2.5	5.0	10
II	2.5	10.0	5
III	2.5	15.0	3

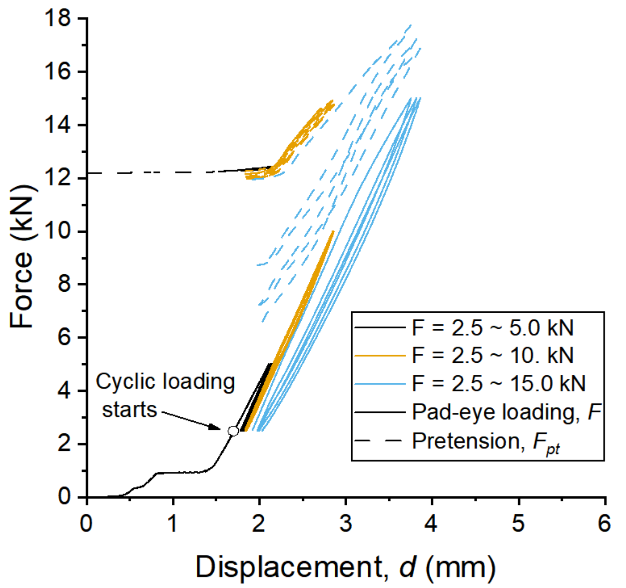

Figure 10 Pad-eye loading and pretension versus pad-eye displacement during cyclic loading at 30°

Figure 10 shows the force – displacement during cyclic loading, as well as the evolution of the pretension force. Permanent displacement is accumulated and pretension is reduced with cyclic loading.

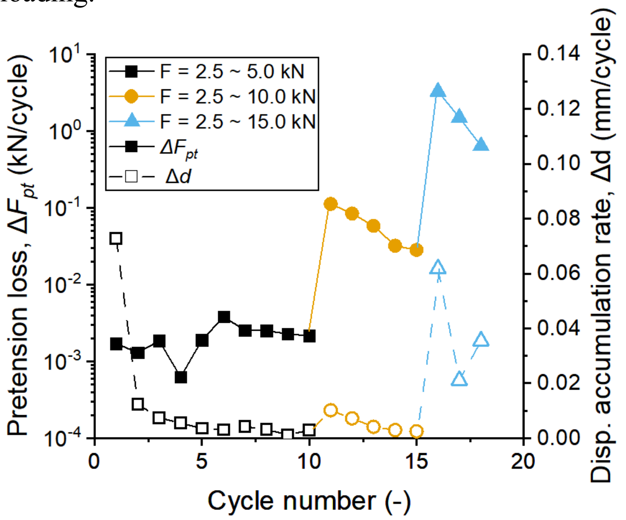

Figure 11 Pretension and pad-eye displacement accumulation rate versus cycle number

Figure 11 shows the loss of pretension ΔP_{PT}, which is defined as the pretension at the minimum force in each cycle minus by pretension at the minimum force in the last cycle, the varying with cycle number. The displacement accumulation rate Δd, which is defined similarly to ΔP_{PT}, is also shown in Figure 11.

In Loading Packet I (maximum force = 5 kN), ΔP_{PT} and Δd become stable and remain minimal after a limited number of cycles. Compared to Packet I, the increase in the maximum force to 10 kN in Packet II leads to an increase in ΔP_{PT} by approximately two orders of magnitude, reaching values on the order of 0.01–0.1 kN per cycle, while the displacement accumulation rates Δd remains of the same order as in Packet I. When the maximum force is increased to 15 kN (Packet III), the loss of pretension becomes substantial and ΔP_{PT} in the first cycle exceeds 1 kN/cycle.

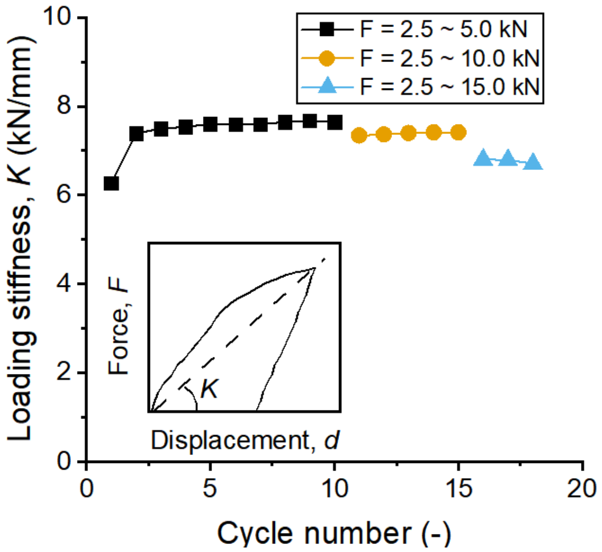

Figure 12 Loading stiffness of model SA varying with cycle number

The loading stiffness K, defined as secant slope of the pad-eye force – displacement response, is also assessed as shown in Figure 12. The first cycle exhibits a lower K value than the subsequent cycles. For helical piles, which may be considered analogues of SAs, although they are typically deployed in soils, a similarly reduced stiffness in the first loading cycle has been widely reported. This behaviour has been attributed to densification of the soil above the helical bearing plate (Schiavon et al. 2017; Wang et al. 2025). By analogy, the observed response in the present tests may suggest a local compaction/interlocking of the rock material above the anchor fingers during the initial loading cycle.

In Packet I and II, the loading stiffness K slowly increases with cycle number, potentially due to progressively local compaction above the fingers. Whilst Packet III exhibits K values decreasing with number may be attributed to reduction of pretension. This reduction of loading stiffness corresponds to the unstable displacement accumulation shown in Figure 11.

4 CONCLUSIONS

By small scale 1g physical modelling, this paper investigates cyclic loading performance of a novel groutless rock anchor system for offshore renewable energy applications, namely the Swift Anchor (SA) in soft calcarenite rock.

The SA is characterised by a self-drilling installation process and the mobilisation of resistance through mechanical interlocking with the surrounding rock via an expandable bottom finger. To activate the mechanical interlocking, pretension is required by applying torque at the top end of the anchor. The 1g experiments adopted a combination of a Hilti HDA-P M10, a top taper, and a pad-eye, to model the SA.

When applying pretension, the pretension – torque is initially linear and may become non-linear with increase in magnitude of the pretension. A similar trend is also observed on pure axial loading – displacement response of the sole Hilti HDA-P M10 anchor. The non-linear behaviour may indicate instigation of localised rock damage developed during loading. Such a non-linear response occurs when the axial force exceeds approximately 8 kN. The pretension force decreases with time, due to cessation of applying torque and mechanical relaxion in the anchor model in a short term and due to soft rock and rock/anchor interface creep in a longer term. Up to 50 Nm torque was applied, resulting in up to 15 kN pretension, which decreased to a relatively stable value of approximately 12 kN after 40 minutes, although the pretension appeared to infinitely reduce at a minimal rate in the adopted soft rock. Further studies are required to investigate a boarder range of ground conditions regarding the creep effects.

Following application of pretension, cyclic loading tests were conducted on a model SA at a loading diction of 30° from seabed surface. The cyclic loading was conducted in three packets. The minimum loading was constantly 2.5 kN and the maximum loading was 5.0, 10.0 and 15.0 kN, respectively, in each packet.

The rate of permanent displacement accumulation and the rate of pretension loss with cyclic loading increased with increasing the applied cyclic loading magnitude. When the maximum loading was no more than 10 kN, the loss of pretension was moderate and loading stiffness remained stable or even slowly increased with number of cycles. When the maximum loading of 15 kN was applied, substantial pretention loss and progressive stiffness degradation with number of cycles were exhibited, accompanied by significant displacement accumulation.

Further studies could be conducted to investigate the effects of varying initial pretension magnitude and loading direction. Advanced numerical simulations are also encouraged to elucidate the underlying mechanisms governing the observed macroscopic behaviour.

ACKNOWLEDGEMENTS

The authors are grateful for the financial support provided by Supergen Offshore Renewable Energy (ORE) Hub through the Flexible Funding scheme (FF2024-1076 – Effect of creep and tensile cyclic loads on serviceability of rock anchoring systems for floating ORE mooring).

REFERENCES

Brown, E. T. (2015). Rock engineering design of post-tensioned anchors for dams – A review. *Journal of Rock Mechanics and Geotechnical Engineering*, 7(1), 1-13. https://doi.org/10.1016/j.jrmge.2014.08.001

Buckley, R. M., Jardine, R. J., Kontoe, S., Liu, T., Byrne, B. W., McAdam, R. A., Schranz, F., and Vinck, K. (2024). Axial cyclic loading of piles in low-to-medium-density chalk. *Géotechnique*, 74(6), 570-583. https://doi.org/10.1680/jgeot.22.00044

Cerfontaine, B., Brown, M., Caton, A., Hunt, A., and Cresswell, N. (2021). Numerical modelling of rock anchor uplift capacity for offshore applications. In *Proceedings of 14th European Wave & Tidal Energy Conference*, Plymouth, UK, 5-9, Sep.

Ciantia, M., Wang, W., Previtali, M., Kaufmann, N., and Cresswell, N. (2026). Three-dimensional numerical modelling of Swift Anchor for offshore renewable energy applications. In Proceedings of 21st International Conference on Soil Mechanics and Geotechnical Engineering, Vienna, Austria. International Society of Soil Mechanics and Geotechnical Engineering, vol. (accepted).

Cook, R. A., Doerr, G. T., and Klingner, R. E. (1989). *Design guide for steel-to-concrete connections*.

Finnie, I., Gillinder, R., Richardson, M., Erbrich, C., Wilson, M., Chow, F., Banimahd, M., and Tyler, S. (2019). Design and Installation of Mobile Offshore Drilling Unit Mooring Piles using Innovative Drive-Drill-Drive Techniques. In *Proceedings of 13th Australia - New Zealand Conference on Geomechanics*, Perth, Australia.

Genco, A. (2025). *Development of a novel rock anchoring system for floating offshore renewable energy mooring*. PhD, University of Dundee.

Genco, A., Ciantia, M. O., Previtali, M., Brown, M., Ivanovic, A., Cresswell, N., and Twomey, V. (2024a). Large deformation numerical assessment of rock anchor response under axial loading for offshore renewable energy applications. *Computers and Geotechnics*, 173. https://doi.org/10.1016/j.compgeo.2024.106563

Genco, A., Ciantia, M. O., Previtali, M., Brown, M. J., Ivanovic, A., Cresswell, N., and Twomey, V. (2024b). A small-scale physical model for evaluating the axial response of Rock Anchors for offshore renewable applications. In *Proceedings of 5th European Conference on Physical Modelling in Geotechnics*, Delft, the Netherlands, Oct., 2-4. https://doi.org/10.53243/ECPMG2024-130

Grindheim, B., Li, C. C., Høien, A. H., and Lia, L. (2023). Behavior of a Rock Mass in Uplift Field Tests of Rock Anchors. *Rock Mechanics and Rock Engineering*, 57(4), 2339-2364. https://doi.org/10.1007/s00603-023-03689-2

Jonak, J., Karpinski, R., Wojcik, A., and Siegmund, M. (2021). The Influence of the Physical-Mechanical Parameters of Rock on the Extent of the Initial Failure Zone under the Action of an Undercut Anchor. *Materials (Basel)*, 14(8). https://doi.org/10.3390/ma14081841

Kaufmann, N., Jeffcoate, P., Cresswell, N., and Ciantia, M. (2025). Full-Scale Load Testing of the Swift Rock Anchor. In *Proceedings of 16th European Wave and Tidal Energy Conference*, Madeira, Portugal, 7–11, Sep. https://doi.org/10.36688/ewtec-2025-1018

Kim, H. K., and Cho, N. J. (2012). A design method to incur ductile failure of rock anchors subjected to tensile loads. *Electronic Journal of Geotechnical Engineering*, 17, 2737–2746.

ORE Catapult, and ARUP (2024). Floating offshore wind anchor review.

Riccio, T. (2025). *Experimental observations on the behaviour of axially and laterally loaded piles installed in soft rock*. PhD, University of Dundee.

Schiavon, J. A., Tsuha, C. H. C., and Thorel, L. (2017). Cyclic and post-cyclic monotonic response of a single-helix anchor in sand. *Géotechnique Letters*, 7(1),11-17. 10.1680/jgele.16.00100

Sandrini, L., Ciantia, M. O., Castellanza, R., Bridi, I., Grassi, D., Balconi, G., & Perrone, P. (2022). GFRP anchoring systems for soft-rock geostructures with high cultural and environmental value. In R. Lancellotta, C. Viggiani, A. Flora, F. de Silva, & L. Mele (Eds.), *Geotechnical Engineering for the Preservation of Monuments and Historic Sites III* (1 ed., pp. 1173-1183). CRC Press. https://doi.org/10.1201/9781003308867-94

Wang, W., Brown, M. J., Sharif, Y. U., Davidson, C., and Ciantia, M. O. (2025). Centrifuge Modeling of the Installation Advancement Ratio Effect on the Cyclic Response of a Single-Helix Screw Pile for Floating Offshore Wind. *Journal of Geotechnical and Geoenvironmental Engineering*, 151(1). https://doi.org/10.1061/JGGEFK.GTENG-12331